Scaling of Optogenetically Evoked Signaling in a Higher-Order Corticocortical Pathway in the Anesthetized Mouse

Xiaojian Li[1], Naoki Yamawaki[1], John M. Barrett[1], Konrad P. Körding[1,2,3] and Gordon M. G. Shepherd[1]*

[1] Department of Physiology, Feinberg School of Medicine, Northwestern University, Chicago, IL, United States, [2] Department of Physical Medicine and Rehabilitation, Feinberg School of Medicine, Northwestern University, Chicago, IL, United States, [3] Department of Bioengineering, School of Engineering and Applied Science, University of Pennsylvania, Philadelphia, PA, United States

Quantitative analysis of corticocortical signaling is needed to understand and model information processing in cerebral networks. However, higher-order pathways, hodologically remote from sensory input, are not amenable to spatiotemporally precise activation by sensory stimuli. Here, we combined parametric channelrhodopsin-2 (ChR2) photostimulation with multi-unit electrophysiology to study corticocortical driving in a parietofrontal pathway from retrosplenial cortex (RSC) to posterior secondary motor cortex (M2) in mice *in vivo*. Ketamine anesthesia was used both to eliminate complex activity associated with the awake state and to enable stable recordings of responses over a wide range of stimulus parameters. Photostimulation of ChR2-expressing neurons in RSC, the upstream area, produced local activity that decayed quickly. This activity in turn drove downstream activity in M2 that arrived rapidly (5–10 ms latencies), and scaled in amplitude across a wide range of stimulus parameters as an approximately constant fraction (~0.1) of the upstream activity. A model-based analysis could explain the corticocortically driven activity with exponentially decaying kernels (~20 ms time constant) and small delay. Reverse (antidromic) driving was similarly robust. The results show that corticocortical signaling in this pathway drives downstream activity rapidly and scalably, in a mostly linear manner. These properties, identified in anesthetized mice and represented in a simple model, suggest a robust basis for supporting complex non-linear dynamic activity in corticocortical circuits in the awake state.

Keywords: corticocortical, electrophysiology, silicon probe, optogenetics, channelrhodopsin, modeling

INTRODUCTION

Corticocortical pathways support inter-areal communication, which is central to behavior (Felleman and Van Essen, 1991; Mišić and Sporns, 2016). Quantitative characterization of signaling in corticocortical pathways is essential for understanding and modeling how they contribute to information-processing. This information can also help to address a fundamental question in connectomics research, of how the relatively static structure of corticocortical networks can give

rise to the complex non-linear dynamic activity typically observed in awake animals (Park and Friston, 2013). For example, it is unknown whether such non-linearities are present already at the most basic level of the intrinsic biophysical properties of corticocortical connections, or whether they arise at higher levels of network interactions.

Connectomics studies have identified a structural basis for many corticocortical pathways (Oh et al., 2014; Zingg et al., 2014; Jbabdi et al., 2015), and optogenetic mapping studies have begun to characterize dynamic signaling at the mesoscopic scale (Lim et al., 2012). However, the properties of inter-areal signaling in these pathways have been challenging to resolve *in vivo*, particularly in higher-order pathways, which are many synapses removed from the sensory periphery and thus difficult to analyze in an isolated, selective, and spatiotemporally precise manner with natural stimuli. Extracellular electrical stimulation has been used in efforts to artificially generate focal activity, but is inherently limited due to its non-specificity, antidromic activation, and other issues (Nowak and Bullier, 1998; Histed et al., 2009).

Recently developed optogenetic methods hold promise for overcoming these limitations. Such methods have enabled detailed characterization of cell-type-specific connections in long-range circuits *ex vivo* (Petreanu et al., 2007, 2009). Corticocortical circuits in mice have begun to be characterized at the cellular level with this approach (Mao et al., 2011; Hooks et al., 2013; Yang et al., 2013; Kinnischtzke et al., 2014, 2016; Petrof et al., 2015; Suter and Shepherd, 2015; Sreenivasan et al., 2016), mostly focusing on lower-order corticocortical pathways that involve primary cortical areas. In parallel are efforts to use similar approaches *in vivo* to characterize how optogenetically evoked activity interacts with sensory input at the level of primary sensory cortex (e.g., Manita et al., 2015; Reinhold et al., 2015).

Among these newly characterized corticocortical circuits, however, is a higher-order projection from retrosplenial cortex (RSC) to posterior secondary motor cortex (M2) (Yamawaki et al., 2016). RSC axons innervate M2 neurons broadly across all layers and projection classes, forming a synaptic circuit whereby RSC, which receives input from dorsal hippocampal networks and is involved in spatial memory and navigation, appears to communicate with M2, which sends output to diverse motor-related areas and appears to be involved in diverse sensorimotor functions. As such, this connection is an interesting target for the reverse engineering of signaling properties in a higher-order inter-areal corticocortical pathway.

Here we have developed an approach based on combining the slice-based circuit analysis methods (Yamawaki et al., 2016) with system-identification methods used in sensory systems research (Wu et al., 2006) to develop an *in vivo* paradigm suitable for assessing and manipulating corticocortical circuit dynamics in the intact brain. We used the same labeling paradigms to express ChR2 in presynaptic RSC neurons, and developed *in vivo* methods in the ketamine-anesthetized mouse for sampling photo-evoked multi-unit activity in M2 driven by RSC photostimulation. Duplication of the setup to permit both stimulation and recording at both ends of the RSC→M2 projection allowed a detailed parametric characterization

of both local (upstream) and downstream activity evoked both ortho- and antidromically. This allowed us to systematically investigate how optogenetically evoked RSC→M2 signaling drives downstream activity as a function of upstream stimulation amplitude and duration. The parametric nature of the data collected with this approach allowed us to also assess the linearity of corticocortical signaling in this pathway.

MATERIALS AND METHODS

Animals
Studies were approved by the Northwestern University Animal Care and Use Committee, and followed the animal welfare guidelines of the Society for Neuroscience and National Institutes of Health. Wild-type mice (*Mus musculus*, C57BL/6, female and male; Jackson Laboratory, Bar Harbor, ME) were bred in-house. Mice were 6–9 weeks old at the time of *in vivo* experiments.

Cortical Injections
Mice under deep anesthesia with inhaled isoflurane underwent stereotaxic injection of adeno-associated virus (AAV) carrying ChR2 into the RSC, following standard methods as previously described (Yamawaki and Shepherd, 2015; Yamawaki et al., 2016). The two viruses and constructs that were used were AAV1-CAG-ChR2-Venus (AAV1.CAG.ChR2-Venus.WPRE.SV40, AV-1-20071P, University of Pennsylvania Vector Core, Philadelphia, PA; Addgene #20071, Addgene, Cambridge, MA) and AAV9-CaMKII-hChR2-eYFP (AAV9.CamKIIa.hChR2(H134R)-eYFP.WPRE.hGH, AV-9-26969P, University of Pennsylvania Vector Core; Addgene #26969P). Stereotaxic coordinates for the RSC were: −1.4 mm caudal to bregma, ∼0.5 mm lateral to midline. To minimize cortical damage, the glass injection pipette was pulled to a fine tip, beveled to a sharp edge (Micro Grinder EG-400, Narishige, Tokyo, Japan), and advanced slowly into the cortex; injections were made slowly (over 3 min) at two depths (0.8 and 1.2 mm from pia, ∼20 nL per injection). Mice received post-operative analgesic coverage (0.03 mg/kg buprenorphine pre-operatively, 1.5 mg/kg meloxicam once every 24 h for 2 days, buprenorphine for 1 day post-operatively) to minimize pain and discomfort. Mice were maintained for at least 3 weeks prior to experiments, to allow time for ChR2 expression levels to rise in the infected neurons. Data presented in **Figures 3–7** are from a total of 6 mice injected with the AAV9-CaMKII-hChR2-eYFP, and 6 with the AAV1-CAG-ChR2-Venus vectors. Animal numbers for other experiments are given in the results sections and figures. In a small subset of experiments, the same injector system was used to inject drugs into the cortex during the recording session (100 nL volumes, injected over 2 min). Viral methods followed institutional guidelines for safe handling and utilization.

In Vivo Circuit Analysis: Surgical Procedures
As the first step in the *in vivo* recording session, mice underwent placement of cranial mounting hardware. Mice were deeply anesthetized with inhaled isoflurane and placed in a stereotaxic frame, and small skin incision was made over the cerebellum

to expose the cranium. A spade terminal (non-insulated, 69145K438, McMaster-Carr, Elmhurst, IL), with a stainless-steel set screw (single-ended #8-32, SS8S050, Thorlabs, Newton, NJ) crimped into its hole, was affixed to the cranial surface with dental cement (Jet Denture Repair Powder, Lang Dental Manufacturing Co., Inc., Wheeling, IL). The set screw was later screwed into the tapped hole located at the top of a 1/2″ optical post (Thorlabs), for head fixation. The time for head-post-mounting and dental cement hardening was ~30 min. Mice were then transitioned from isoflurane to ketamine-xylazine (ketamine 80–100 mg/kg and xylazine 5–15 mg/kg, injected intraperitoneally), remaining deeply anesthetized during the transition. They were transferred to the recording apparatus, and head-fixed using the set screw as described above. Body temperature was monitored with a rectal probe and maintained at ~37.0°C via feedback-controlled heating pad (FHC, Bowdoin, ME). Craniotomies were opened over the RSC and M2 using a dental drill (EXL-M40, Osada, Los Angeles, CA), just large enough (~1 mm) to allow passage of the linear arrays and the tips of the optical fibers. During the subsequent recordings, ACSF (containing, in mM, 127 NaCl, 25 $NaHCO_3$, 1.25 NaH_2PO_4, 2.5 KCl, 25 D-glucose; all reagents from Sigma-Aldrich, St Louis, MO) was frequently applied to the exposed brain area to prevent damage from dehydration. The level of anesthesia was continuously monitored based on paw pinching, whisker movement, and eye-blinking reflex. Additional doses of anesthesia were given subcutaneously (ketamine-xylazine 50% of induction dose) when required, typically every 40–50 min over the duration of the experiment, which was typically ~3 h.

Photostimulation Apparatus

An optical fiber (FG400AEA, multimode fiber, 0.22 NA, 400 μm core, outer diameter 550 μm with coating; Thorlabs), mounted on a motorized micromanipulator (Sutter Instrument, Novato, CA), was positioned directly over the region of the infected neurons in the RSC. The tip of the fiber was ~0.5 mm away from the surface of the brain, immersed in ACSF. In most experiments, a second fiber was similarly positioned directly over the M2. For each fiber, the light source was an LED (M470L3, Thorlabs), coupled to the fiber by an adapter (SM1SMA, Thorlabs). The power was controlled using an LED driver (LEDD1B, Thorlabs; or, driver based on RCD-24-1.00 module, RECOM Lighting, Neu-Isenburg, Germany). The output power of the LED driver was modulated by signal waveforms delivered via a multifunction analog and digital interface board (NI USB 6229; National Instruments, Austin, TX) or by a signal generator based on a 32-bit microcontroller board (Arduino Due with ARM Cortex-M3, Adafruit, New York, NY). The boards were also used to send a short pulse train to digitally encode the start and other parameters of the light waveform, sampled on the digital input port of the electrophysiology data acquisition (DAQ) board. Software tools (LabVIEW) included a GUI (GenWave) for generating and transferring the waveforms to the LED controller. The LED driver was either internally software-triggered (GenWave) or externally hardware-triggered by a digital signal. A power meter was used to calibrate the relationship between input voltage to the driver and the output intensity of the fiber,

and the calibration curve was used to determine the voltages (in the range of 0–5 V) corresponding to 0, 20, 40, 60, 80, and 100% of the full power (6.1 mW, measured at the tip of the optical fiber). During the experiment, analog voltages corresponding to these intensities were sent to the LED driver.

Electrophysiology Apparatus and Procedures

The linear arrays used were 32-channel silicon probes with ~1 MΩ impedance and 50-μm spacing (model A1×32–6mm-50–177, NeuroNexus, Ann Arbor, MI), in either "triangular" or "edge" configuration. The probes were mounted on a motorized 4-axis micromanipulator (Thorlabs MTSA1 linear translator mounted on a Sutter MP285 3-axis manipulator), and positioned under stereoscopic visualization over the M2 at cortical surface (i.e., entry point) coordinates of +0.6 mm rostral to bregma and 0.2 mm lateral to midline. The probes were tilted by ~30° off the vertical axis for alignment with the radial axis of the cortex. The probe was then slowly inserted into the cortex at a rate of 2 μm/s (controlled by software) to a nominal depth of 1,600 μm from the pia. However, as described below (see "Laminar analysis" section), the actual depth was slightly less (by ~250 μm), due to the viscoelastic properties of the brain tissue, leaving ~5 contacts outside the brain. In most experiments, a second array was similarly inserted into the RSC (same stereotaxic coordinates as given above for the viral injections), except that in this case the array was inserted perpendicular to the horizontal plane, and the optical fiber was slightly tilted. In some experiments, probe tracks were labeled by coating the probe with fluorescent dye, and subsequently visualized in brain slices with epifluorescence optics to verify accurate placement of the probes in the M2 and/or RSC.

Signals were amplified using an amplifier board based on a RHD2132 digital electrophysiology interface chip (Intan Technologies, Los Angeles, CA). The RHD2132 chip is an analog front end that integrates the analog instrument amplifiers, filters, analog-to-digital (ADC) converters, and microcontrollers in one chip. The serial peripheral interface (SPI) port is used to configure the chip and to stream the silicon probe data to the data acquisition (DAQ) board. The gain of the amplifier was fixed at $96 \times 2 = 192$ (2-stage amplifier). The filter was set to an analog bandpass of 0.1~ 7.5 K Hz with a digital filter cutoff of 1 Hz. Because the 32 channels of the silicon probe inputs share the same 16 bit ADC with a multiplexer, and the maximum sample rate of the ADC is 1.05×10^6 samples per second (SPS), the single channel sample rate was set to 30,000 SPS.

For hardware control, we used a RHD2000 USB Interface Evaluation Board (Intan) or DAQ board based on a breakout board with a XEM6010 USB/FPGA module (Opal Kelly, Portland, OR), a field-programmable gate array (FPGA) with many digital I/O channels for communicating with other digital devices and streaming in the linear array data from the RHD2000 amplifiers. The USB port of the module was linked with a USB cable to pipe the data stream in or out of the PC. The RHD2000 amplifier boards were connected to a DAQ board using SPI interface cables in low-voltage differential signal mode, which is well suited for communication via longer cables. In this

experiment, the digital ports included in the DAQ board were only used for acquiring the LED photostimulation parameters from the LED controller.

For data logging, The C++/Qt based experimental interface evaluation software (Intan) was used for early stage evaluation. Then the original APIs (Rhythm USB/FPGA interface) were all rebuilt and wrapped up into a LabVIEW-based SDK. All the software, including the amplifier configuration, online visualization, data logging, and more, were developed from this SDK in LabVIEW environment.

Trace Acquisition and Analysis

With the mouse anesthetized and head-fixed and the two linear arrays and two optical fibers in place, photostimuli were repeatedly delivered while continuously sampling electrophysiological activity across the 32 channels per array. In each trial, a single photostimulus was delivered on one fiber, using one of the 25 combinations of stimulus intensities (20, 40, 60, 80, or 100 percent of maximum) and durations (1, 5, 10, 20, or 50 ms). Across all trials, all 25 stimulus combinations were tested, in randomly interleaved sequence, with an inter-trial (interstimulus) interval of 2 s, This cycle was repeated many (e.g., ~30) times, and the entire process was repeated again for the second optical fiber (if present). For stimulation on each fiber, the resulting electrophysiological data set typically consisted of 2 arrays × 32 channels/array × 25 stimulus parameter combinations × 30 trial repetitions = 48,000 traces.

These trace data were stored as the raw signal from the amplifiers, and filtered as follows. A digital 60 Hz notch filter (Matlab, Mathworks, Natick, MA) was used to reduce line hum. A digital high-pass filter (800 Hz cut-off, 2nd-order Butterworth; Matlab) was used to isolate the higher-frequency components of the electrophysiological responses for event detection.

For event detection, in this study we focused on analyzing multi-unit activity; although single units could be isolated on some channels, single-unit analysis was generally hampered by the short-latency barrage of activity just after a photostimulus, particularly in the upstream area and especially at higher stimulus intensities. Similar to previous studies of multi-unit activity, we defined "events" (i.e., spikes in the traces) as voltage excursions that were ≥4 standard deviations (s.d.) above the baseline amplitude (measured in the 1,500 ms prior to the stimulus), lasting ≥0.1 ms (3 continuous samples) in duration. Event detection based on these criteria was performed on all traces using Matlab routines.

Peristimulus time histograms were constructed as follows, using Matlab routines. For each trial, time stamps were determined for each detected event, and the time stamps of all the events of every channel were used to generate a single-trial raster plot using 1-ms bins. Trials were repeated multiple times, and raster plots were grouped by experimental condition (e.g., each particular stimulus parameter combination) and averaged over all trials (typically ~30 trials) to obtain a multi-trial histogram showing the mean activity across all channels for that condition. The multi-trial histograms were also summed across channels to obtain an all-channel histogram for each condition (**Figure 1G** bottom).

The raw traces were contaminated by a brief stimulus artifact immediately after stimulus onset and offset. These transients were greatly attenuated by digital high-pass filtering (described above). The duration of the residual transients was estimated for each experiment (i.e., animal), and ranged from 1 to 3 ms. For display, both transients were simply blanked for this brief duration. For subsequent analyses, the data were replaced in the following way, taking advantage of the availability of responses recorded using different stimulus durations. For the onset transient, the event count of the blanked window was replaced by the average value of the baseline window over the 20 ms pre-stimulus interval. For the offset transient, the event count of the blanked window was replaced by the event count measured for the next-longer-duration stimulus acquisition. For example, in the case a 2-ms-long transient in the responses recorded during a 10-ms-long stimulus, the data over the interval of 11–12 ms post-stimulus (i.e., the 11th and 12th 1-ms bins) were replaced by the data value recorded at 11–12 ms during the 20-ms-long stimulus, and so on. However, for the longest-duration stimulus of 50 ms, we instead replaced with the baseline values, as post-stimulus activity had returned to approximately baseline levels by this time.

Laminar Analysis

For all linear probe recordings the nominal depth of probe insertion into the cortex was nominally 1,600 μm, based on the total displacement of the motorized manipulator holding the probe. However, due to the viscoelastic properties of the brain tissue, the actual depth of insertion was slightly less, as mentioned above. For the subset of studies examining the laminar profile of activity, we sought additional estimates of the depth of insertion. With a stereomicroscope we visualized the entry point of the silicon probe into the brain at higher magnification, finding that ~5 contacts were still exposed. We also found, empirically, that the electrophysiological traces could be used to estimate the depth of insertion, based on the variance over time in the FFT (20–60 Hz band) of each channel's voltage traces (0.5 s duration), which showed a transition from low-variance exterior channels to high-variance intracortical channels. The depth estimated by this approach matched well with that based on images of the electrode at the site of penetration into the brain. Using this combination of approaches, the estimated depths of each channel used in the laminar analysis were thus likely to be accurate within 50–100 μm.

Ex vivo acute brain slice recordings from M2 neurons were performed using previously described photostimulation and electrophysiology methods (Yamawaki et al., 2016). Recordings were made at 34°C in cell-attached configuration with the amplifier in voltage-follower mode, using borosilicate pipettes filled with ACSF. A blue LED was used to deliver wide-field photostimuli (5 ms duration, 1.0 mW mm^{-2} specimen-plane intensity, presented every 30 s, 5 sweeps per neuron) through a low-power (4×) objective lens. In each slice, for a total of two slices per animal, recordings were made sequentially from one pyramidal neuron in layer 2/3 and one in layer 5, varying the order from slice to slice. The lens was centered identically over M2 during each recording (rather than centering it over each

neuron), so as to activate the same set of axons. Traces were analyzed to determine the average spike probability per sweep.

Model Based Analysis

We fit the following model to the locally evoked activity (i.e., the set of 25 median all-channel histograms over all mice injected with the same viral construct) in RSC:

$$A_{RSC}(t-u) = ms(t) / \left| a_0 + \sum_{\Delta t}^{T} s(t-\Delta t) \right| \quad (1)$$

where m is a scaling factor, a_0 regulates the strength of decay, Δt indexes the delays over which stimulation affects activity ($\Delta t = 0$ would be instantaneous activation), $s(t)$ is the optical stimulus and u is the delay. The three parameters of this model u, m, and a_0 were optimized to minimize the root mean squared error (RMSE) of the model using the MATLAB fminsearch function.

We fit the following model to the downstream activity in M2:

$$A_{M2}(t) = \vartheta \left(m \sum_{\Delta t=1}^{T} e^{\frac{-\Delta t}{\tau_{interact}}} A_{RSC}(t-\Delta t) - \theta \right) + c \quad (2)$$

where m is a scaling factor, $\vartheta(x) = 0$ for $x < 0$ and $\vartheta(x) = x$ for $x \geq 0$, Δt indexes the past input from RSC, $\tau_{interact}$ is the interaction time constant, $A_{RSC}(t)$ is the activity in area RSC, θ is the threshold, and c is the baseline. The four parameters of this model c, θ, $\tau_{interact}$, and m were also optimized to minimize the RMSE.

Experimental Design and Statistical Analysis

The main data set comes from an experimental design involving parametric stimulation and recording that will be explained in detail in the Results. In general, unless otherwise stated, the
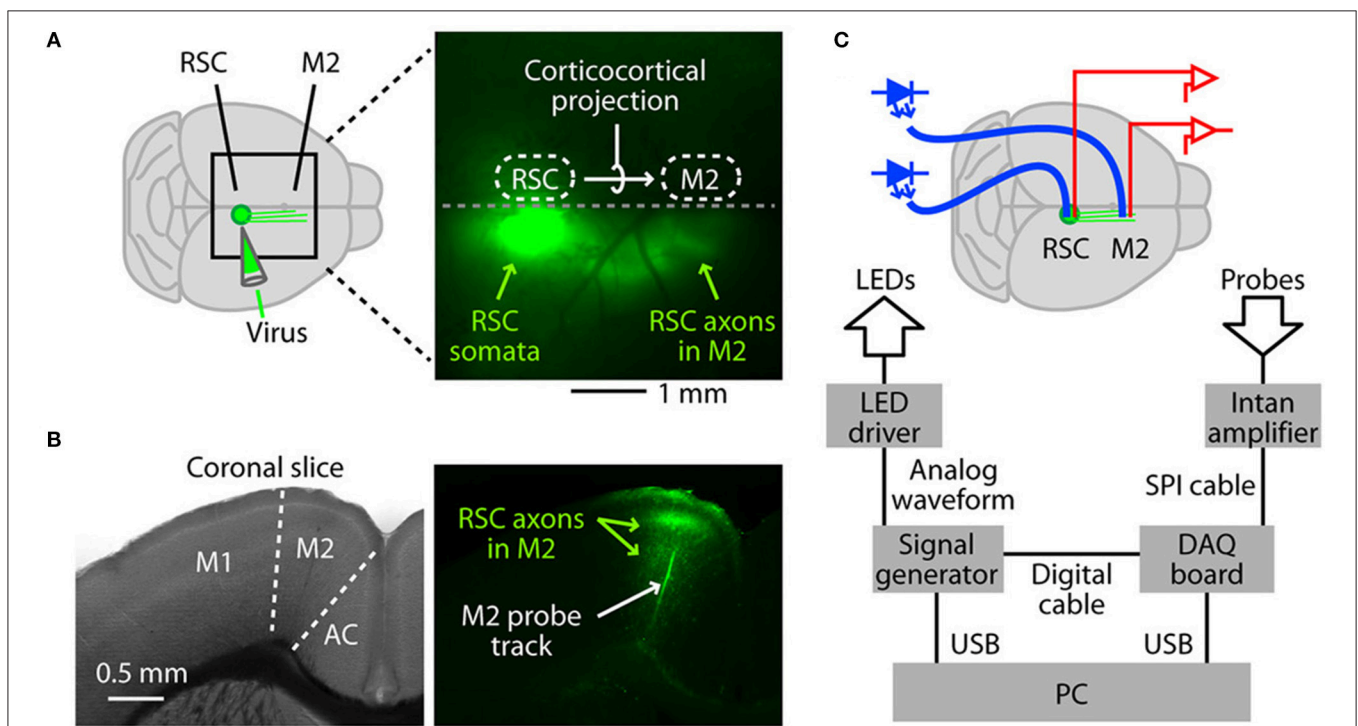

FIGURE 1 | Experimental paradigm for characterizing inter-areal signaling in the corticocortical projection from retrosplenial (RSC) to posterior secondary motor (M2) cortex. **(A)** Virus injection in RSC infects somata at the injection site, resulting in anterograde labeling of RSC axons projecting to M2. Right: epifluorescence image of the dorsal surface of the brain of an anesthetized mouse, showing labeled axons projecting from RSC to posterior M2. **(B)** Coronal brain slices showing labeled axons in M2, and the track of a dye-coated linear array. Left: bright-field image. M2 is between the primary motor (M1) and anterior cingulate (AC) cortices. Right: epifluorescence image, showing labeled axons from RSC within M2, and the track of a dye-coated linear array (probe) that had been inserted in M2. **(C)** Depiction of experimental set-up showing aspects of the hardware control apparatus and wiring. An optical fiber (blue) was placed over, and a silicon probe was inserted into, each of the two cortical areas. The optical fibers were coupled to blue light-emitting diodes (LEDs). For clarity, only the fiber over the RSC is depicted here. See Methods for additional details. **(D-G)** Examples of RSC recordings during RSC photostimulation. **(D)** Raw (unfiltered) traces from the 32-channel linear array in the RSC, recorded during a single trial of RSC photostimulation (10 ms pulse, 100% intensity). The stimulus is indicated by the bar above, and by the blue box. The interior line with in the box indicates the 3-ms post-stimulus time point, which was the maximal width of the responses that were blanked to eliminate a stimulus artifact. The region demarcated by the black box is shown in the inset at the bottom. **(E)** Same, but after high-pass filtering. **(F)** Traces from a single channel, recorded on multiple stimulus presentations. Photostimulation reliably generated post-stimulus activity. **(G)** Top: Raster plot of detected events for a single trial (traces shown in **E**). Middle: Histogram showing events detected across all trials for each channel. Bottom: Overall histogram, calculated by summing across all channels. **(H-K)** Same as **(D-G)**, for the recordings made simultaneously from the linear array inserted in M2. **(L)** Histograms for the RSC recordings, for 25 combinations of stimulus durations (1, 5, 10, 20, and 50 ms) and intensities (20, 40, 60, 80, and 100% of maximum). **(M)** Same, for the M2 recordings.
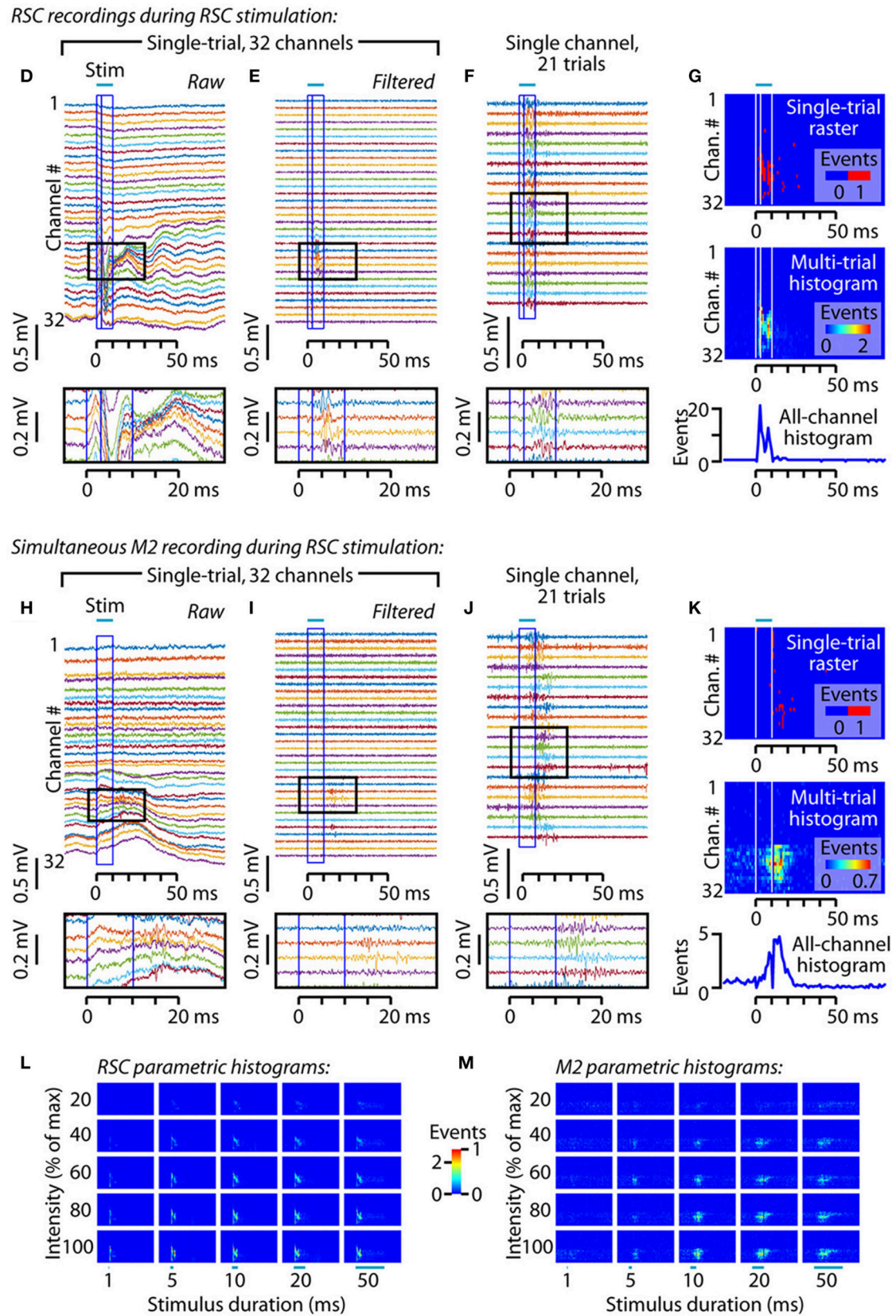
FIGURE 1 | (Continued).

following statistical methods were used. Descriptive statistics are reported and displayed as sample medians ± median absolute deviations (m.a.d.) (calculated with the Matlab function, mad.m). Group data are compared using appropriate non-parametric tests (e.g., rank sum tests for unpaired and sign tests for paired data) as indicated, with significance defined as $p < 0.05$.

RESULTS

RSC Photostimulation Drives Downstream M2 Activity

To investigate corticocortical signaling in the RSC→ M2 pathway, we used viral methods to label the RSC neurons with ChR2, optical fibers to photostimulate them, and linear arrays to record the evoked activity. Similar to previous studies of this pathway (Yamawaki et al., 2016), we infected neurons in RSC with an AAV encoding ChR2 and a fluorescent protein (**Figures 1A,B**). After a recovery period of several weeks, animals were anesthetized with ketamine and underwent placement of a photostimulation fiber over the RSC and silicon probes in both the RSC and M2 (**Figure 1C**). (As described at the end of the Results, a second optical fiber was also routinely placed over the M2 to enable antidromic activation; however, the main focus of the study is on the "forward" orthodromic signaling evoked by RSC stimulation.)

With this optogenetic photostimulation and electrophysiological recording arrangement, we photostimulated ChR2-expressing neurons in RSC and sampled responses simultaneously in RSC (**Figures 1D-G**) and M2 (**Figures 1H-K**). The raw traces (**Figures 1D,H**) were high-pass filtered (**Figures 1E,I**), revealing brief barrages of photo-evoked events on multiple channels on both probes, easily discernable in single trials. Over repeated trials, photostimulation reliably evoked spiking activity on channels showing responses (**Figures 1F,J**). We analyzed the traces to detect events, representing multi-unit activity (see Methods), and used the timing of events to construct single-trial rasters and multi-trial peristimulus time histograms (**Figures 1G,K**). These histograms showed robust, transient increases in multi-unit activity starting with a short delay after the onset of photostimulation in RSC, for both the RSC and M2 recordings. The example traces and histograms are for responses to a photostimulus with 10 ms duration and maximal intensity, extracted from a much larger data set using 25 different combinations of stimulus durations and intensities (**Figures 1L,M**).

Prior to presenting our analyses of these parametric data sets in detail in later sections, we present some additional characterizations of the technique. One consideration is whether responses differ for different viruses and constructs, and we therefore performed parallel experiments with two different AAV serotypes carrying different variants of ChR2 driven by different promoters: AAV1-CAG-ChR2-Venus, carrying wild-type ChR2 driven by the CAG promoter, for expression in most types of cortical neurons; and, AAV9-CaMKII-hChR2-eYFP, carrying ChR2 with the H134R mutation driven by the CaMKII promoter, which is specific for excitatory neurons
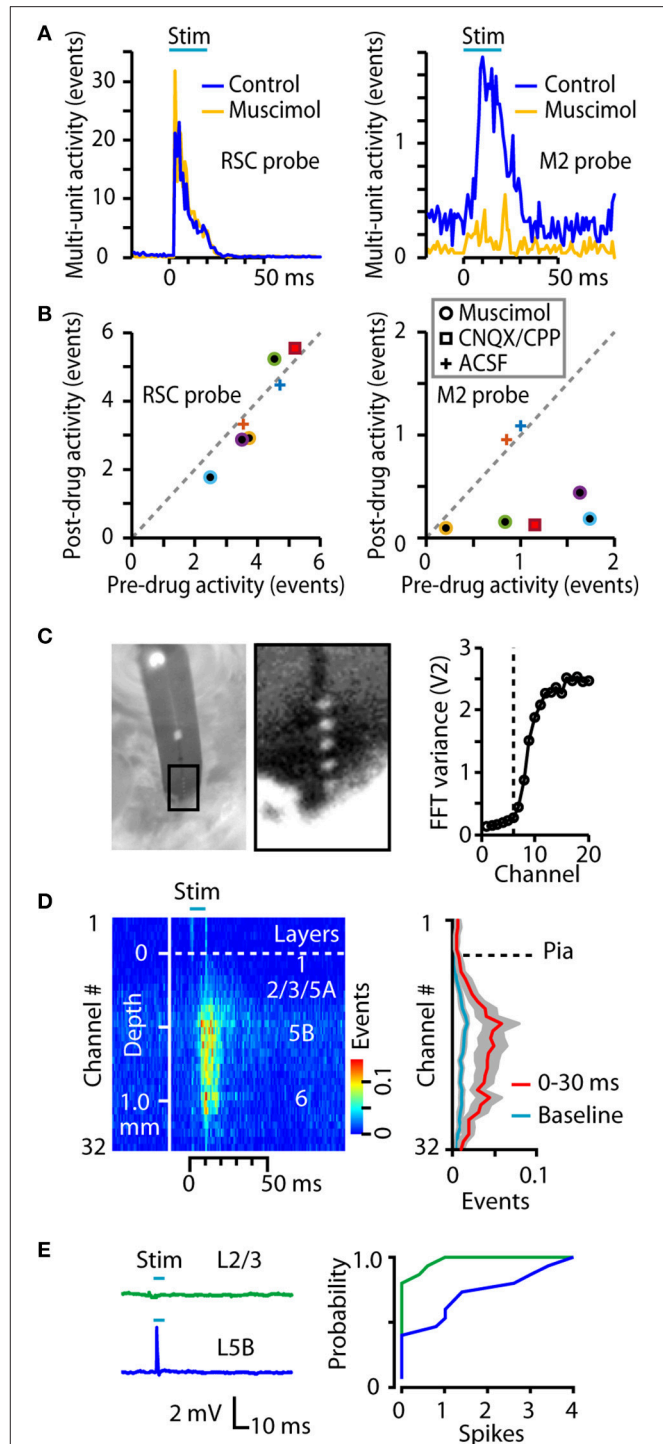
FIGURE 2 | Additional characterizations of the technique. **(A)** Example histograms for responses to RSC stimulation, recorded before and after injection into M2 of muscimol. Muscimol, which suppresses synaptically driven activity, greatly reduced downstream activity in M2 (right) but not in RSC (left). **(B)** Responses recorded before and after injection into M2 of muscimol, CNQX/CPP, or ACSF (see legend for symbols). Drug injection did not affect activity in RSC (left) but significantly reduced responses in M2 (right; $p = 0.013$, t-test, $n = 5$). Colors indicate different experiments (animals). **(C)** Left: Image of
(Continued)

FIGURE 2 | 32-channel silicon probe, taken through the ocular of a stereoscope, showing 5 visible contacts above the penetration site into the cortex. Distance between contacts is 50 μm. Right: Plot of the variance in the FFT of the traces collected on the first 20 channels of the probe, showing an abrupt increase for channels deeper than the 6th contact (dashed line). **(D)** Left: Average peristimulus-time histogram across all channels in a 32-channel array in M2 during RSC photostimulation, plotted on a color scale (mean ± s.e.m., for $n = 9$ mice injected with AAV1-CAG-ChR2-Venus). Right: Average laminar profile, plotted as the average event rate per channel during the response interval (red) and baseline (blue). **(E)** In *ex vivo* brain slice experiments, cell-attached recordings were made from layer 2/3 and layer 5B neurons while photostimulating RSC axons. Left: Example traces showing spiking response in the layer 5B neuron. Right: The mean number of evoked spikes was calculated for each neuron, and plotted as a cumulative histogram of spike probability. Layer 5B neurons spiked significantly more than layer 2/3 neurons ($p = 0.009$, rank-sum test; median spikes were 0 vs. 1 for layer 2/3 vs. 5B, respectively; $n = 15$ layer 2/3 and 15 layer 5B neurons, recorded from 6 slices obtained from 3 animals).

(see Methods). The two viruses gave very similar responses (as described in later sections), suggesting that our strategy is not overly affected by the particular types of viruses and opsin constructs used. Both viruses infected cortical neurons only locally at the injection site in the RSC, without evidence of retrograde infection in M2, as shown previously (Yamawaki et al., 2016); i.e., the M2 contained anterogradely labeled axons of RSC neurons, but not retrogradely labeled somata of M2 neurons.

The brief burst of multi-unit activity observed in M2 (**Figures 1I-K**) arriving shortly after that in RSC (**Figures 1E-G**) suggests that spiking activity in RSC neurons propagated via their corticocortical axons and synaptically drove spiking activity in M2 neurons, via the abundant excitatory RSC→M2 connections previously described for this corticocortical circuit (Yamawaki et al., 2016). Alternatively, events detected in M2 might represent spikes in presynaptic axons rather than in post-synaptic neurons. However, this seems unlikely, particularly as spikes in thin corticocortical axons are much smaller in amplitude and usually difficult to detect (Raastad and Shepherd, 2003). To assess whether the M2 responses primarily reflect synaptically driven spikes of post-synaptic M2 neurons, rather than spikes in presynaptic axons, we sampled M2 responses before and after injecting M2 with muscimol (100 nL, 5 mM in ACSF), a GABA agonist, which suppresses spiking in cortical neurons while preserving presynaptic spiking (Chapman et al., 1991; Chatterjee and Callaway, 2003). We also simultaneously recorded the activity in RSC, to control for the possibility that muscimol injected into M2 might diffuse to RSC. As expected, muscimol injection in M2 had no effect on activity in RSC but abolished most of the activity in M2 (**Figure 2A;** 4 of 4 animals). A similar effect was observed when blockers of glutamatergic synaptic transmission (100 nL of 1 mM CNQX and 5 mM CPP in ACSF) was injected in M2 (1 animal). Pooling the muscimol and CNQX/CPP data showed no effect of the drugs on RSC activity but a significant effect on M2 responses (**Figure 2B**; $p = 0.013$, t-test, $n = 5$ animals). Injection of saline had no effect (2 of 2 animals). Thus, M2

responses appear to be primarily driven by corticocortical synaptic activity.
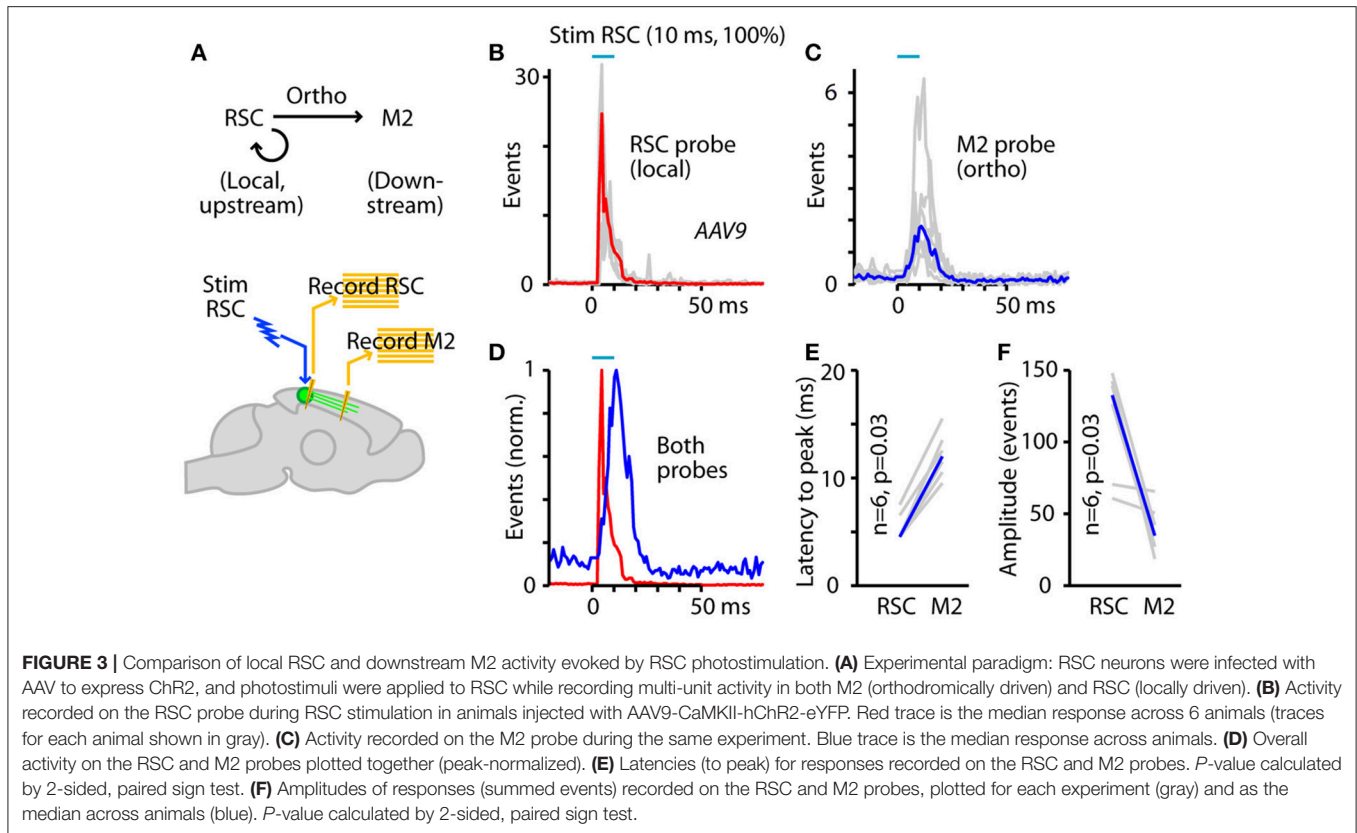
We considered the sensitivity of the results to probe placement. In earlier pilot experiments the probe was sometimes inadvertently placed slightly lateral by ∼0.5–1 mm, resulting in recordings in M1 instead of M2. In this case we observed little or no photo-evoked activity, consistent with the anatomy and electroanatomy of the RSC→M2 projection, which provides little or no direct input to M1 neurons (Yamawaki et al., 2016). Thus, accurate probe placement is important, but inaccurate placement would simply decrease the observed activity.

We also considered the laminar profile of M2 activity. To estimate the depth of penetration of the silicon probes (32 channels and 50 μm spacing), they were inserted leaving ∼5 contacts out of the cortex, as verified both by viewing the site of entry with a high-power stereoscope, and assessing channel noise variance, which was low for contacts outside cortex (see Methods) (**Figure 2C**). Group analysis ($n = 9$ mice injected with AAV1-CAG-ChR2-Venus) indicated wide distribution of activity across channels, and thus cortical layers, albeit with a bias toward middle and deeper layers (**Figure 2D**). Previous slice-based characterization of RSC→M2 connectivity indicated that RSC axons form monosynaptic excitatory synapses onto post-synaptic M2 neurons across all layers and major classes of projection neurons, including upper-layer neurons (Yamawaki et al., 2016). Because those experiments were performed in whole-cell voltage-clamp mode, here, to explore the cellular basis for the relatively lower activation of upper layers in M2 we performed similar brain slice experiments but with cell-attached current-clamp recordings, allowing assessment of the efficacy of RSC inputs in generating suprathreshold (spiking) activity in M2 neurons. Comparison of layer 2/3 and layer 5 neurons showed significantly greater tendency of photo-activated RSC axons to generate spikes in layer 5 neurons (**Figure 2E**), consistent with the laminar profile recorded *in vivo*.

From the results of these initial characterizations we conclude that (i) optogenetically stimulating RSC drives a delayed, brief wave of spiking activity in M2; (ii) the evoked activity appears to reflect mostly the properties of the corticocortical circuit itself rather than the those of the viruses and/or constructs; (iii) the M2 activity appears to arise from orthodromically driven signaling along the RSC→M2 corticocortical pathway, rather than non-specific (e.g., cortex-wide) activation; and (iv) RSC drives M2 neurons across multiple layers, particularly the middle and deeper layers. Next, we turned to a more in-depth analysis of recordings made simultaneously in both cortical areas.

Comparison of Local RSC and Downstream M2 Activity Evoked by RSC Photostimulation

Recording simultaneously from both the RSC and M2 during RSC photostimulation allowed us to assess both the locally driven activity in upstream RSC and the orthodromically driven activity in downstream M2 (**Figure 3A**). For clarity, here we present

FIGURE 3 | Comparison of local RSC and downstream M2 activity evoked by RSC photostimulation. **(A)** Experimental paradigm: RSC neurons were infected with AAV to express ChR2, and photostimuli were applied to RSC while recording multi-unit activity in both M2 (orthodromically driven) and RSC (locally driven). **(B)** Activity recorded on the RSC probe during RSC stimulation in animals injected with AAV9-CaMKII-hChR2-eYFP. Red trace is the median response across 6 animals (traces for each animal shown in gray). **(C)** Activity recorded on the M2 probe during the same experiment. Blue trace is the median response across animals. **(D)** Overall activity on the RSC and M2 probes plotted together (peak-normalized). **(E)** Latencies (to peak) for responses recorded on the RSC and M2 probes. *P*-value calculated by 2-sided, paired sign test. **(F)** Amplitudes of responses (summed events) recorded on the RSC and M2 probes, plotted for each experiment (gray) and as the median across animals (blue). *P*-value calculated by 2-sided, paired sign test.

only the data obtained using a stimulus of 100% intensity and 10 ms duration. With RSC photostimulation the activity recorded locally in RSC rose rapidly at the onset of photostimulation, peaking at approximately 5 ms, and declined rapidly as well (**Figure 3B**). That the peak response occurred shortly after the brief post-stimulus blanking interval (from 0 to maximally 3 ms, depending on the experiment; used to eliminate a photovoltaic transient, as described in Methods) suggests that the blanking procedure affected primarily the rising phase of the response waveform. Activity recorded simultaneously in M2 (**Figure 3C**) followed with a brief latency (7.5 ms after the RSC peak for AAV9-CaMKII-hChR2-eYFP, and 6.5 ms for AAV1-CAG-ChR2-Venus; **Figures 3D,E**) and rose to lower levels than observed in RSC (RSC/M2 amplitude ratio: 3.8 for AAV9-CaMKII-hChR2-eYFP, 4.1 for AAV1-CAG-ChR2-Venus; **Figure 3F**).

The results of this two-probe characterization of RSC photostimulation thus reveal two important aspects of corticocortical driving in this pathway. First, at the upstream end there is a rapid and strong decay of the local activity in the directly photostimulated RSC. The time course and extent of this decay are consistent with ChR2 desensitization (Nagel et al., 2003, 2005; Lin et al., 2009), although other factors such as activation of interneurons and activity-dependent synaptic depression are also likely to contribute. Second, at the downstream end, the corticocortically driven activity in M2 was reduced in amplitude and slightly delayed relative to the RSC activity. A caveat is that these properties might not be generalizable, reflecting instead the particular

photostimulus parameters used in these experiments. Therefore, we next investigated in detail the stimulus dependence of the responses by exploring a wide range of stimulus intensities and durations.

Parametric Characterization of Orthodromic (Forward) Driving

Key parameters for the dynamics of a circuit are the dependency on stimulus amplitude (light intensity) and duration (pulse width). Stimulus trials were delivered at five different intensities (20, 40, 60, 80, and 100% relative to maximum) and durations (1, 5, 10, 20, and 50 ms), with random interleaving and many repetitions (typically ∼30 trials per experiment) for each of the 25 unique intensity-duration combinations (**Figure 4A**). Responses were averaged across trials as before, and 25 histograms for the responses on the local RSC probe (**Figure 4B**) and the downstream M2 probe (**Figure 4C**) were calculated as the median across animals. Clearly, the evoked activity in both RSC and M2 varied with stimulus parameters. To assess how response properties might depend systematically on stimulus parameters, we developed a simple model, and performed several further analyses.

A Simple Two-Stage Model Captures the Major Features of Orthodromic Driving

Visual inspection of the waveforms of both the RSC and M2 responses (**Figures 4B,C**) showed roughly linear increases with

FIGURE 4 | Parametric characterization of orthodromic (forward) driving. **(A)** Light pulses with a total of 25 different combinations of stimulus intensities (20, 40, 60, 80, and 100% relative to maximum) and durations (1, 5, 10, 20, and 50 ms) were used to photostimulate the RSC. **(B)** Activity recorded locally in RSC (red) in response to RSC photostimulation using the stimuli shown in **(A)**. Each trace is the median response across animals with AAV9-CaMKII-hChR2-eYFP ($n = 6$ experiments). **(C)** Activity recorded simultaneously in M2 (green) in the same experiments.
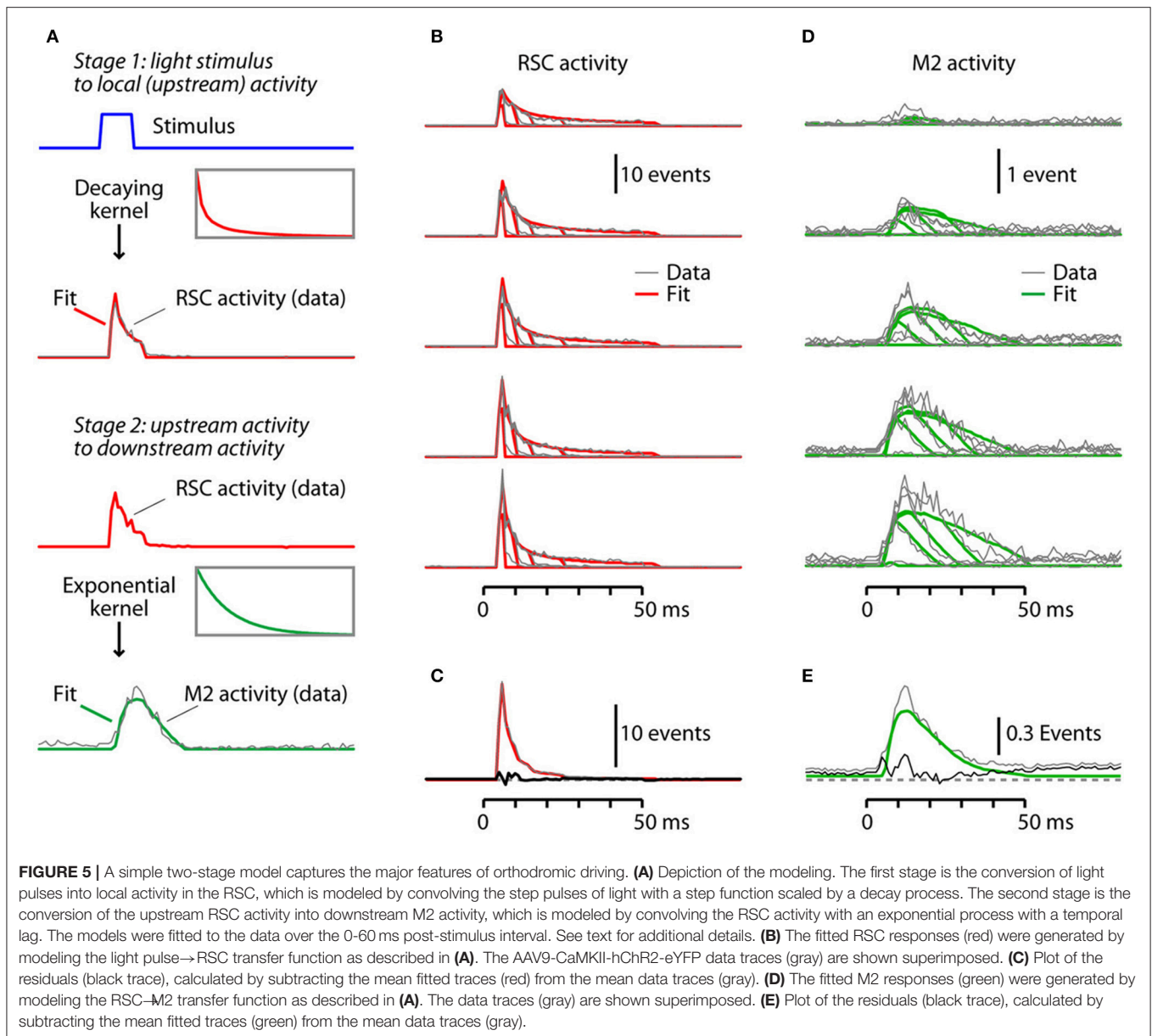
intensity. Clearly, activity in the photostimulated RSC decays rapidly, consistent with ChR2 densensitization (as discussed above). However, in the downstream M2, it is unclear how responses scale with upstream RSC activity; for example, do they scale linearly, or show signs of adaptation? We would like a simple model to allow us to both describe and interpret the data.

Explorative data analysis revealed that we could fit the 25 histograms of activity in the directly stimulated (upstream) area well with briefly delayed activation followed by a large and rapid decay (**Figure 5A**). Hence, we modeled the response as a time-shifted delta function divided by a linear function of the integral of the stimulus history. So this first-stage model has 3 parameters for gain, delay, and the steady-state adaptation. These parameters seem intuitively necessary: the gain describes the strength of the locally generated activity; the delay is needed due to the ~3 ms blanking of the stimulus artifact (see Methods), but can also account for the kinetics of ChR2 activation and spike generation; and some degree of adaptation (of the locally generated activity) is expected from ChR2 inactivation/desensitization kinetics, and allows for additional factors contributing to a temporal decline in activity (e.g., GABA release, synaptic depression).

Indeed, we found this first-stage model to produce good fits when we analyzed activity in the stimulated (RSC) area. We find that the model qualitatively describes the data, describing both its initial peak and its decay over time (**Figures 5B,C**). The first-stage model does not capture the initial 3 ms (which were

blanked), but since response amplitudes peaked later than this the model nevertheless captured the main features of the response. Moreover, the first-stage model has high R^2-values on both the AAV9-CaMKII-hChR2-eYFP (0.93) and the AAV1-CAG-ChR2-Venus (0.83) datasets. This suggests that the stimulation effect is largely described by a linear, essentially immediate translation of the ChR2-mediated depolarization into spiking activity, which decays rapidly.

Next, we developed a second-stage model for the corticocortical driving of M2 activity by RSC activity. Explorative data analysis revealed that 25 histograms of activity in M2, the indirectly stimulated (downstream) area, could be fit well in terms of the activity of the stimulated area simply using thresholded activation, without an additional decay or adaptation process (**Figure 5A**). We modeled this by convolving the upstream activity with an exponentially decaying kernel and applying a threshold. So this second-stage model has 4 parameters for gain, threshold, kernel time-constant, and baseline. These 4 parameters again seem intuitively necessary: the gain describes the strength of the corticocortically driven downstream activity; the threshold accounts for the inability of insufficiently strong upstream stimulation to produce any downstream activity; there is a slow transmission of information; and, there is non-zero baseline activity in the downstream area. Adding an explicit delay parameter to the second-stage model was not necessary: the combination of thresholding and slow stimulus integration sufficed to reproduce the experimentally observed the delay.

FIGURE 5 | A simple two-stage model captures the major features of orthodromic driving. **(A)** Depiction of the modeling. The first stage is the conversion of light pulses into local activity in the RSC, which is modeled by convolving the step pulses of light with a step function scaled by a decay process. The second stage is the conversion of the upstream RSC activity into downstream M2 activity, which is modeled by convolving the RSC activity with an exponential process with a temporal lag. The models were fitted to the data over the 0-60 ms post-stimulus interval. See text for additional details. **(B)** The fitted RSC responses (red) were generated by modeling the light pulse→RSC transfer function as described in **(A)**. The AAV9-CaMKII-hChR2-eYFP data traces (gray) are shown superimposed. **(C)** Plot of the residuals (black trace), calculated by subtracting the mean fitted traces (red) from the mean data traces (gray). **(D)** The fitted M2 responses (green) were generated by modeling the RSC→M2 transfer function as described in **(A)**. The data traces (gray) are shown superimposed. **(E)** Plot of the residuals (black trace), calculated by subtracting the mean fitted traces (green) from the mean data traces (gray).
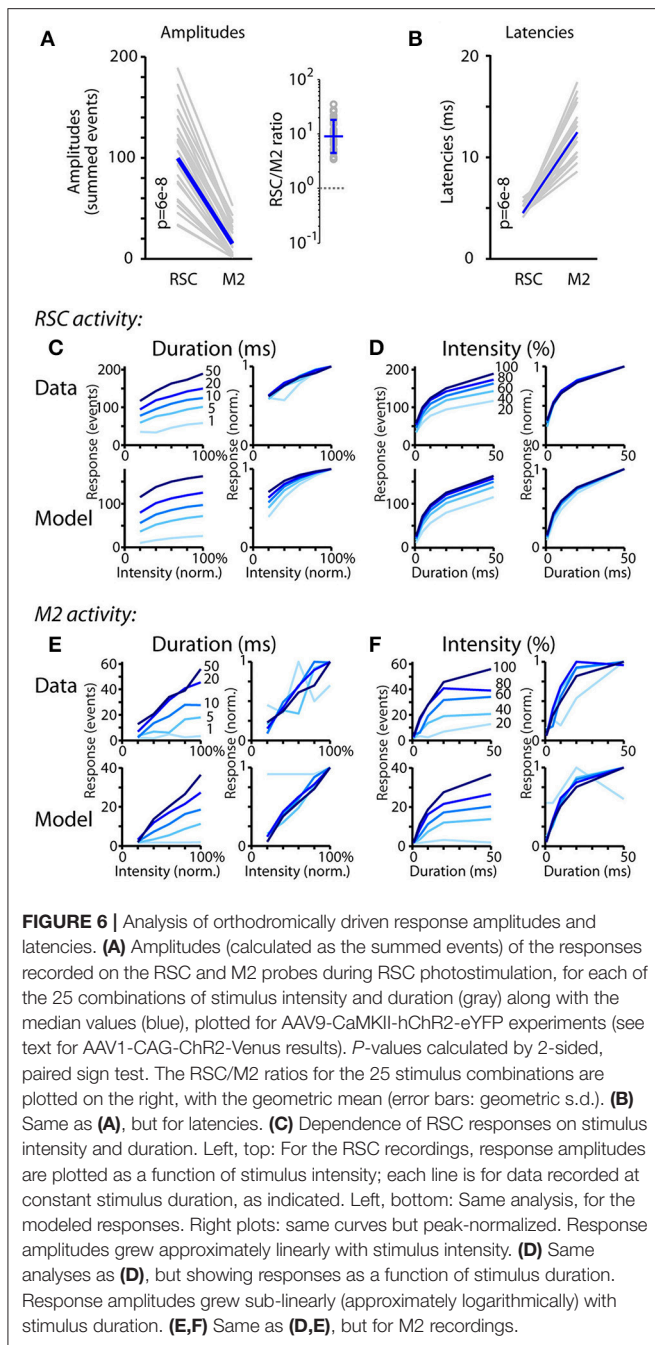
We found this second-stage model to produce good fits in the downstream (M2) area. We find that the model qualitatively describes the data, describing both its slow rise, and its subsequent decay over time (**Figures 5D,E**). It also describes how in some conditions there is no activation whatsoever. This model also has high R^2-values on both the AAV9-CaMKII-hChR2-eYFP (0.70) and the AAV1-CAG-ChR2-Venus (0.65) datasets. The time constants of the fitted exponential kernels were on the order of a few tens of milliseconds (20 ms for AAV9-CaMKII-hChR2-eYFP and 32 ms for AAV1-CAG-ChR2-Venus data), which may include contributions from many aspects, such as synaptic current and membrane time constants. It is also comparable to the time constants of fast spike adaptation in cortical excitatory neurons (La Camera et al., 2006; Wark et al., 2007; Suter et al., 2013). Thus the bulk of the response in the downstream area, M2,

is described by linear integration of the input from the upstream area, RSC, with an effect that decays exponentially over time.

Analysis of Orthodromically Driven Responses

Next, we assessed whether the reduced amplitude of M2 responses (compared to upstream RSC activity, discussed above) was a consistent property across stimulus parameters. Plotting the response amplitudes in RSC and M2 for all 25 stimulus combinations showed that these ranged widely but with a consistent relationship, substantially greater in RSC than in M2 (**Figure 6A**). The same pattern was observed for both viruses (average ratios of RSC/M2 amplitude across stimulus combinations: for AAV9-CaMKII-hChR2-eYFP, geometric mean = 9.0, geometric s.d. = 2.0; for AAV1-CAG-ChR2-Venus,

FIGURE 6 | Analysis of orthodromically driven response amplitudes and latencies. **(A)** Amplitudes (calculated as the summed events) of the responses recorded on the RSC and M2 probes during RSC photostimulation, for each of the 25 combinations of stimulus intensity and duration (gray) along with the median values (blue), plotted for AAV9-CaMKII-hChR2-eYFP experiments (see text for AAV1-CAG-ChR2-Venus results). *P*-values calculated by 2-sided, paired sign test. The RSC/M2 ratios for the 25 stimulus combinations are plotted on the right, with the geometric mean (error bars: geometric s.d.). **(B)** Same as **(A)**, but for latencies. **(C)** Dependence of RSC responses on stimulus intensity and duration. Left, top: For the RSC recordings, response amplitudes are plotted as a function of stimulus intensity; each line is for data recorded at constant stimulus duration, as indicated. Left, bottom: Same analysis, for the modeled responses. Right plots: same curves but peak-normalized. Response amplitudes grew approximately linearly with stimulus intensity. **(D)** Same analyses as **(D)**, but showing responses as a function of stimulus duration. Response amplitudes grew sub-linearly (approximately logarithmically) with stimulus duration. **(E,F)** Same as **(D,E)**, but for M2 recordings.

geometric mean = 9.2, geometric s.d. = 1.7), even though absolute response amplitudes were generally stronger for AAV9-CaMKII-hChR2-eYFP compared to AAV1-CAG-ChR2-Venus (1.5-fold for RSC responses and 2.1-fold for M2 responses; $p < 10^{-3}$, sign test). Thus, activity in the downstream area, M2, was generally about a tenth of that in RSC, across a wide range of stimulus parameters.

Of further importance to the interaction are latencies. These also showed a consistent relationship, with M2 responses peaking with a short delay after RSC responses (**Figure 6B**). The same pattern was observed for both viruses (median
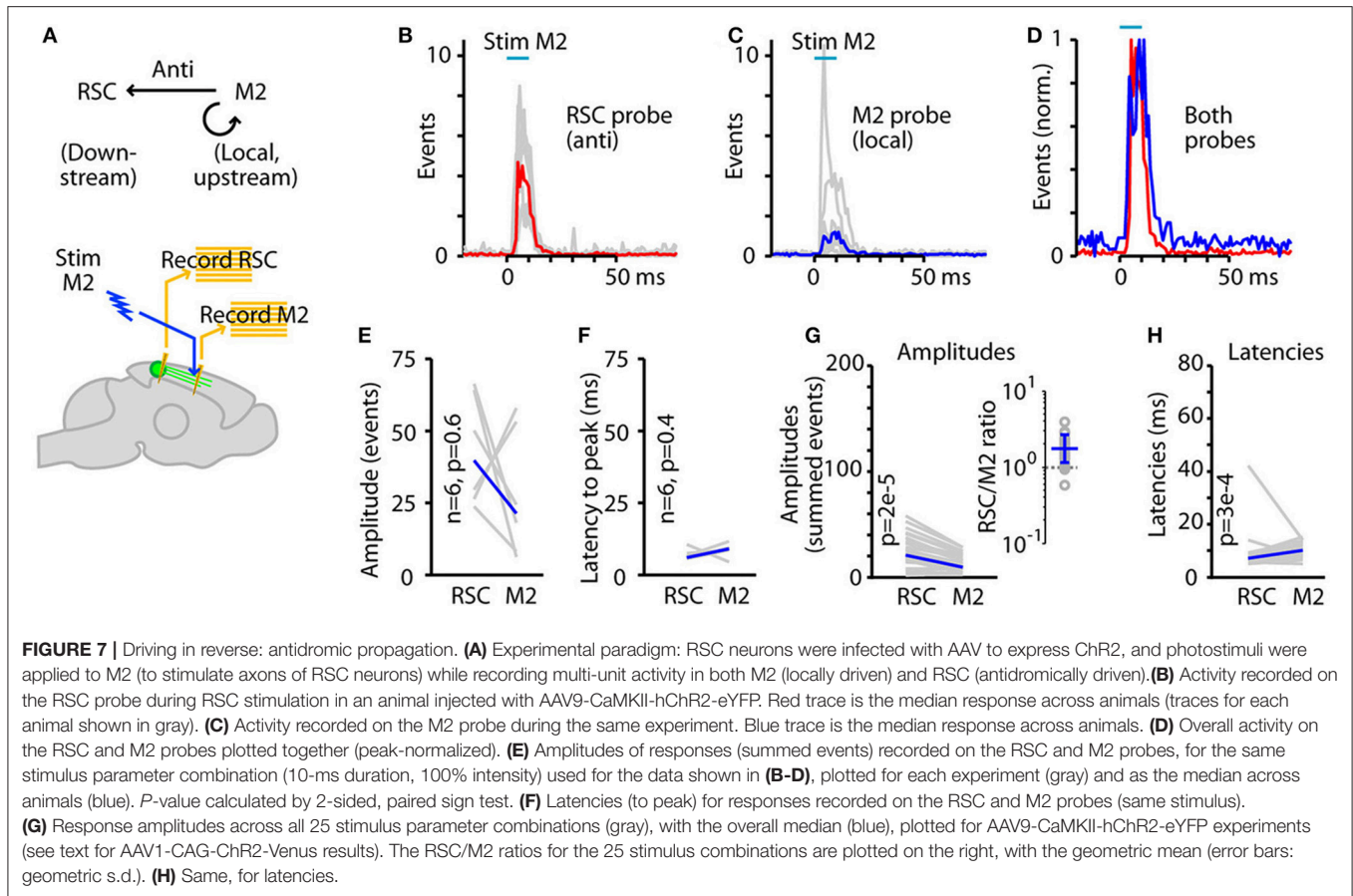
latency of M2 response relative to RSC response of 8 ms for AAV9-CaMKII-hChR2-eYFP and 7 ms for AAV1-CAG-ChR2-Venus experiments). In this case, unlike the absolute response amplitudes, the latencies of the responses in RSC and M2 did not differ significantly for AAV9-CaMKII-hChR2-eYFP vs. AAV1-CAG-ChR2-Venus ($p > 0.05$, sign test). In contrast to the amplitudes, the latencies were largely stimulus-independent. Consistent with this, across all stimulus combinations, peak latency in M2 was uncorrelated with response amplitude in RSC (Spearman's rank correlation coefficient; AAV1-CAG-ChR2-Venus: $R^2 = 0.02$, $p = 0.54$; AAV9-CaMKII-hChR2-eYFP: $R^2 = 0.12$, $p = 0.09$).

Response amplitudes in both areas clearly varied systematically and substantially for different combinations of stimulus intensity and duration, but how? Plotting the RSC responses as a function of stimulus intensity showed a nearly linear dependence (**Figure 6C**). In contrast, plotting the same RSC responses as a function of stimulus duration showed a sub-linear dependence (**Figure 6D**). Applying the same analysis to the modeled traces gave qualitatively similar results (**Figures 6C,D**, bottom row of plots). The M2 responses showed a similar, albeit noisier, set of patterns, with roughly linear intensity-dependence (**Figure 6E**) and sub-linear duration-dependence (**Figure 6F**). Applying the same analysis to the modeled traces again gave qualitatively similar results (**Figures 6E,F**, bottom row of plots).

Driving in Reverse: Antidromic Propagation

The photoexcitability of ChR2-expressing axons (Petreanu et al., 2007) has previously been exploited in *in vivo* experiments to antidromically drive a transcallosal corticocortical projection (Sato et al., 2014). Here, our experimental set-up (**Figure 1**), by incorporating an optical fiber placed over the M2, allowed us to similarly drive the RSC→M2 projection in reverse, and thereby gain additional insight into signaling properties in this system. Characterization of antidromic optogenetic driving is additionally of technical interest both as an intended (e.g., Sato et al., 2014) or unintended and therefore potentially confounding effect of focal photostimulation in an area containing ChR2-expressing axons. Using the same labeling strategy (i.e., AAV-ChR2 in RSC) and recording (i.e., electrodes in both RSC and M2) arrangement, in the same experiments we also delivered photostimuli to M2 (via a second optical fiber) as a way to activate ChR2-expressing axons there (i.e., projecting from RSC) and thereby gain insight into the properties of antidromic signaling in the same RSC→M2 pathways (**Figure 7A**).

In particular, we wondered if antidromic activation would result in similar or different effects compared to orthodromic activation. Photostimulation in M2 (i.e., of the ChR2-expressing axons of RSC neurons) resulted in a short-latency, short-duration wave of antidromically generated activity in both RSC and a similar but smaller-amplitude wave of locally generated activity in M2 (**Figures 7B-D**). Although neither amplitudes nor latencies differed between RSC and M2 with antidromic activation for the standard (10 ms, 100% intensity) stimulus combination alone (**Figures 7E,F**), when data from all stimulus combinations were pooled the response amplitudes were overall substantially greater in RSC relative to M2 (average ratios of

FIGURE 7 | Driving in reverse: antidromic propagation. **(A)** Experimental paradigm: RSC neurons were infected with AAV to express ChR2, and photostimuli were applied to M2 (to stimulate axons of RSC neurons) while recording multi-unit activity in both M2 (locally driven) and RSC (antidromically driven). **(B)** Activity recorded on the RSC probe during RSC stimulation in an animal injected with AAV9-CaMKII-hChR2-eYFP. Red trace is the median response across animals (traces for each animal shown in gray). **(C)** Activity recorded on the M2 probe during the same experiment. Blue trace is the median response across animals. **(D)** Overall activity on the RSC and M2 probes plotted together (peak-normalized). **(E)** Amplitudes of responses (summed events) recorded on the RSC and M2 probes, for the same stimulus parameter combination (10-ms duration, 100% intensity) used for the data shown in **(B-D)**, plotted for each experiment (gray) and as the median across animals (blue). P-value calculated by 2-sided, paired sign test. **(F)** Latencies (to peak) for responses recorded on the RSC and M2 probes (same stimulus). **(G)** Response amplitudes across all 25 stimulus parameter combinations (gray), with the overall median (blue), plotted for AAV9-CaMKII-hChR2-eYFP experiments (see text for AAV1-CAG-ChR2-Venus results). The RSC/M2 ratios for the 25 stimulus combinations are plotted on the right, with the geometric mean (error bars: geometric s.d.). **(H)** Same, for latencies.

RSC/M2 amplitude across stimulus combinations: for AAV9-CaMKII-hChR2-eYFP, geometric mean = 1.7, geometric s.d. = 1.5; for AAV1-CAG-ChR2-Venus, geometric mean = 3.9, geometric s.d. = 1.7) (**Figure 7G**). Similar to orthodromic stimulation, absolute response amplitudes were generally stronger for AAV9-CaMKII-hChR2-eYFP compared to AAV1-CAG-ChR2-Venus (2.6-fold for RSC responses and 3.8-fold for M2 responses; $p < 10^{-3}$, sign test). Latencies in the two areas were indistinguishable with AAV1-CAG-ChR2-Venus and slightly delayed (by 3 ms) in M2 with AAV9-CaMKII-hChR2-eYFP (**Figure 7H**). Latencies in RSC were slightly shorter with AAV9-CaMKII-hChR2-eYFP than AAV1-CAG-ChR2-Venus (by 2.5 ms; $p < 10^{-4}$, sign test), but those in M2 were the same with the two viruses ($p > 0.05$, sign test). These results indicate that RSC axons forming this corticocortical projection can be robustly activated in M2, generating activity both locally in M2 and antidromically in RSC.

DISCUSSION

We analyzed corticocortical signaling in the RSC→M2 pathway *in vivo* using optogenetic photostimulation and electrophysiology. Across a wide range of stimulus parameters, the downstream responses arrived rapidly and scaled systematically with the photo-evoked activity in the upstream

area. We found that a simple model involving linear integration, delay, and thresholding could describe much of the data.

In using optogenetic photostimulation to analyze this circuit we did not attempt to mimic naturalistic activity patterns of the RSC but rather used this as a tool to drive the circuit in a highly precise, controlled manner (Miesenböck, 2009). This approach allowed us to selectively activate the upstream neurons in the RSC→M2 pathway, and to systematically vary the stimulus intensity and duration and assess whether and how response properties depended on input parameters. Focal optogenetic photostimulation differs fundamentally from non-specific methods for brain stimulation; extracellular electrical stimulation, for example, is inherently limited due to its non-specificity, antidromic activation, and related issues (Histed et al., 2009; Joucla et al., 2012) and could not have been used to selectively study signaling in the RSC→M2 pathway.

Another artificial aspect of these experiments was the use of anesthesia, without which extensive parametric testing would have been challenging with head-fixed animals. Moreover, our studies focused on computational aspects of corticocortical population signaling, not how corticocortical signals relate to the high-dimensional aspects of behavior (Carandini, 2012). In awake animals, even "at rest" the patterns of functional connectivity in the cortex can be extremely complex and

dissimilar to anatomical connectivity, whereas in anesthetized animals the structure-function correspondence is high (Barttfeld et al., 2015). Reduced complexity in the anesthetized state could reflect reduction of non-linearities of corticocortical signaling. Consistent with this possibility, ketamine anesthesia (used here) blocks NMDA receptors, HCN channels, and other molecules involved in highly non-linear forms of signaling in cortical neurons (Chen et al., 2009; Antic et al., 2010; Sleigh et al., 2014). Indeed, a recent study comparing RSC activity in awake vs. ketamine-anesthetized mice found diverse ketamine-associated changes (Fox et al., 2017). Thus, a remaining question is the extent to which the patterns of corticocortical signaling described depend on brain state and anesthetic.

With these caveats, our findings indicate highly linear signaling in the RSC→M2 corticocortical pathway in ketamine-anesthetized mice, when this pathway is probed in an isolated manner. One interpretation is that such signaling represents a kind of stripped-down "ground state" for corticocortical communication in this pathway. We suggest that this simpler, linear mode of corticocortical signaling can serve as a robust basis for complex dynamic activity to emerge in the awake state. Perhaps this provides computational stability and enables simpler algorithms. Similar considerations pertain to thalamocortical pathways, which are likely to be active in the awake state and contribute to non-linear activity by interacting with corticocortical pathways. Further experiments and modeling will be needed to explore such speculations.

We found that a simple two-stage model captured the broad features of the data. At the upstream end, the conversion of light energy into local spiking activity in the upstream area (the RSC) could be described as a simple transfer function dominated by strong and rapid decay. The decay likely reflects primarily ChR2 desensitization, a property common to all ChR2 variants including the two used here (Nagel et al., 2003, 2005; Lin et al., 2009). Additional components of the decay may have come from endogenous factors associated with the neurons and microcircuits in the locally stimulated area (e.g., GABA release from inhibitory interneurons, short-term synaptic depression). One potential application of this first-stage model of the local photoactivation process is that it could be used to design photostimuli that precisely compensate for the decay.

At the downstream end, the conversion of upstream activity (in RSC) into downstream activity (in M2) could be described by a simple exponential process with a brief delay, and no adaptation mechanism. Although a small non-linearity was included in the form of a threshold, the efficacy of the second-stage model suggests that corticocortical signaling is mostly linear. The efficacy of this model implies that corticocortical driving of downstream activity is highly scalable, and furthermore that adaptation (of corticocortical driving) is not a major factor in shaping the downstream response, at least on the short time scales (tens of milliseconds) studied here. However, some contribution of an adaptation process may be reflected in the early component of the responses, which tend to be larger than the fitted traces. Whether this simple model can describe corticocortical signaling in other inter-areal pathways remains to be determined, but similarities between our findings using

optogenetic activation and related work in the visual system (e.g., Carandini et al., 1997) suggest this is plausible.

The scalability of corticocortical signaling observed here may be particular to the RSC→M2 pathway, or may represent a more general computational principle of cortical operation (Miller, 2016; Rolls, 2016). Although cortical circuit organization appears basically conserved, areas can also differ substantially in their quantitative properties (Harris and Shepherd, 2015). Corticocortical signaling in other pathways might therefore be expected to exhibit broadly similar scalability, but with pathway-specific differences in the details of spatiotemporal dynamics. The ability to capture both general and pathway-specific features of corticocortical signaling in a simple mathematical model suggests a utility of this approach both for theoretical approaches to cortical network modeling (Bassett and Sporns, 2017) and for neural engineering approaches in which closed-loop neural dynamics and behavioral control require predictive modeling (Grosenick et al., 2015). Further studies will be needed to test these speculations.

The downstream response latencies (∼8 ms after upstream responses), together with the RSC-M2 inter-areal distance of ∼2 mm and allowing for the timing of synaptic transmission (Sabatini and Regehr, 1999), implies a conduction speed for these RSC→M2 corticocortical axons on the order of 0.3 m/s, a typical value for thin unmyelinated cortical axons (Raastad and Shepherd, 2003). The consistency of the latency timing across different stimulus parameters and lack of correlation with RSC response amplitudes suggests that the RSC→M2 circuit was activated in a similar manner independent of the particular activity level of the RSC neurons; in particular, this suggests that the M2 activity resulted from direct excitatory RSC input to M2 neurons, rather than polysynaptic pathways via posterior parietal cortex or anterior thalamus (Yamawaki et al., 2016) or hippocampus (Sugar et al., 2011). Had polysynaptic interactions been increasingly engaged by longer-duration stimuli, responses should have increased over time, not decreased as observed.

In addition to robust forward (orthodromic) activation, we found robust reverse (antidromic) corticocortical signaling in RSC→M2 circuits. Antidromic driving, evoked by stimulating in M2 the ChR2-labeled axons projecting from RSC, was notable for two distinct properties. First, photostimulation in M2 (of the ChR2-expressing axons of RSC neurons) generated even more activity in RSC than in M2. Thus, the gain in this corticocortical circuit (ratio of RSC to M2 activity) appeared to be a property associated with the anatomical directionality of the projection (RSC→M2), rather than determined by the site of stimulation. The greater activity in RSC than in M2 that was evoked by axonal stimulation in M2 presumably reflects the reliability of antidromic propagation to the soma, and could also reflect locally abundant axonal branches of the labeled RSC neurons. The ratio of RSC/M2 activity generated by antidromic stimulation (roughly 2-fold) was less than that generated by orthodromic stimulation (roughly 10-fold). Multiple factors could contribute to this difference. In particular, stimulation in M2 would directly photo-excite only M2-projecting RSC neurons (antidromically), which are only a subset of the ChR2-expressing neurons in RSC, a potentially much larger fraction of which may be photo-activated

by stimulation in RSC. Second, the efficiency of information transmission appeared roughly similar for anti- and orthodromic stimulation; i.e., a property associated with the site of stimulation rather than the anatomical directionality of the projection. Optogenetic antidromic activation has been previously exploited used as a way to selectively generate activity in an area (e.g., Sato et al., 2014). Our results thus not only provide an additional example of how a corticocortical pathway can be driven in reverse to remotely generate activity in an area of interest, but identify key similarities as well as differences compared to orthodromic driving.

Corticocortical signaling in the RSC→M2 pathway may be critical for conveying information from hippocampus-associated networks involved in spatial memory and navigation to cortical and subcortical networks involved in decision making and action planning and execution (Vann et al., 2009; Sugar et al., 2011; Yamawaki et al., 2016). Consistent with this, lesions of the RSC impair navigation without impairing either motor function or the ability to recognize navigational landmarks (Maguire, 2001), and RSC pathology can be an early and prominent feature of Alzheimer's disease (Minoshima et al., 1997). Conversely, the RSC→M2 connectivity appears strengthened after damage to adjacent cortex in a mouse stroke model (Brown et al., 2009). Thus another potential application of experimental-theoretical paradigm developed here is to understand primary pathology and adaptive plasticity in corticocortical signaling in mouse models of disease.

DATA AVAILABILITY STATEMENT

Data are available upon request.

AUTHOR CONTRIBUTIONS

XL, NY, and GS contributed to the conception and design of the study. XL and NY conducted experiments. XL, JB, and KK analyzed data. KK conceived and designed the computational modeling. All authors contributed to manuscript writing and revision, and read and approved the submitted version.

FUNDING

ACKNOWLEDGMENTS

REFERENCES

Antic, S. D., Zhou, W. L., Moore, A. R., Short, S. M., and Ikonomu, K. D. (2010). The decade of the dendritic NMDA spike. *J. Neurosci. Res.* 88, 2991–3001. doi: 10.1002/jnr.22444

Barttfeld, P., Uhrig, L., Sitt, J. D., Sigman, M., Jarraya, B., and Dehaene, S. (2015). Signature of consciousness in the dynamics of resting-state brain activity. *Proc. Natl. Acad. Sci. U.S.A.* 112, 887–892. doi: 10.1073/pnas.1418031112

Bassett, D. S., and Sporns, O. (2017). Network neuroscience. *Nat. Neurosci.* 20, 353–364. doi: 10.1038/nn.4502

Brown, C. E., Aminoltejari, K., Erb, H., Winship, I. R., and Murphy, T. H. (2009). *In vivo* voltage-sensitive dye imaging in adult mice reveals that somatosensory maps lost to stroke are replaced over weeks by new structural and functional circuits with prolonged modes of activation within both the peri-infarct zone and distant sites. *J. Neurosci.* 29, 1719–1734. doi: 10.1523/JNEUROSCI.4249-08.2009

Carandini, M. (2012). From circuits to behavior: a bridge too far? *Nat. Neurosci.* 15, 507–509. doi: 10.1038/nn.3043.

Carandini, M., Heeger, D. J., and Movshon, J. A. (1997). Linearity and normalization in simple cells of the macaque primary visual cortex. *J. Neurosci.* 17, 8621–8644. doi: 10.1523/JNEUROSCI.17-21-08621.1997

Chapman, B., Zahs, K. R., and Stryker, M. P. (1991). Relation of cortical cell orientation selectivity to alignment of receptive fields of the geniculocortical afferents that arborize within a single orientation column in ferret visual cortex. *J. Neurosci.* 11, 1347–1358. doi: 10.1523/JNEUROSCI.11-05-01347.1991

Chatterjee, S., and Callaway, E. M. (2003). Parallel colour-opponent pathways to primary visual cortex. *Nature* 426, 668–671. doi: 10.1038/nature02167

Chen, X., Shu, S., and Bayliss, D. A. (2009). HCN1 channel subunits are a molecular substrate for hypnotic actions of ketamine. *J. Neurosci.* 29, 600–609. doi: 10.1523/JNEUROSCI.3481-08.2009

Felleman, D. J., and Van Essen, D. C. (1991). Distributed hierarchical processing in the primate cerebral cortex. *Cereb. Cortex* 1, 1–47. doi: 10.1093/cercor/1.1.1

Fox, G. E., Li, M., Zhao, F., and Tsien, J. Z. (2017). Distinct retrosplenial cortex cell populations and their spike dynamics during ketamine-induced unconscious state. *PLoS ONE* 12:e0187198. doi: 10.1371/journal.pone.0187198

Grosenick, L., Marshel, J. H., and Deisseroth, K. (2015). Closed-loop and activity-guided optogenetic control. *Neuron* 86, 106–139. doi: 10.1016/j.neuron.2015.03.034

Harris, K. D., and Shepherd, G. M. G. (2015). The neocortical circuit: themes and variations. *Nat. Neurosci.* 18, 170–181. doi: 10.1038/nn.3917

Histed, M. H., Bonin, V., and Reid, R. C. (2009). Direct activation of sparse, distributed populations of cortical neurons by electrical microstimulation. *Neuron* 63, 508–522. doi: 10.1016/j.neuron.2009.07.016

Hooks, B. M., Mao, T., Gutnisky, D. A., Yamawaki, N., Svoboda, K., and Shepherd, G. M. G. (2013). Organization of cortical and thalamic input to pyramidal neurons in mouse motor cortex. *J. Neurosci.* 33, 748–760. doi: 10.1523/JNEUROSCI.4338-12.2013

Jbabdi, S., Sotiropoulos, S. N., Haber, S. N., Van Essen, D. C., and Behrens, T. E. (2015). Measuring macroscopic brain connections *in vivo*. *Nat. Neurosci.* 18, 1546–1555. doi: 10.1038/nn.4134

Joucla, S., Branchereau, P., Cattaert, D., and Yvert, B. (2012). Extracellular neural microstimulation may activate much larger regions than expected by simulations: a combined experimental and modeling study. *PLoS ONE* 7:e41324. doi: 10.1371/journal.pone.0041324

Kinnischtzke, A. K., Fanselow, E. E., and Simons, D. J. (2016). Target-specific M1 inputs to infragranular S1 pyramidal neurons. *J. Neurophysiol.* 116, 1261–1274. doi: 10.1152/jn.01032.2015

Kinnischtzke, A. K., Simons, D. J., and Fanselow, E. E. (2014). Motor cortex broadly engages excitatory and inhibitory neurons in somatosensory barrel cortex. *Cereb. Cortex* 24, 2237–2248. doi: 10.1093/cercor/bht085

La Camera, G., Rauch, A., Thurbon, D., Lüscher, H. R., Senn, W., and Fusi, S. (2006). Multiple time scales of temporal response in pyramidal and fast spiking cortical neurons. *J. Neurophysiol.* 96, 3448–3464. doi: 10.1152/jn.00453.2006

Lim, D. H., Mohajerani, M. H., Ledue, J., Boyd, J., Chen, S., and Murphy, T. H. (2012). *In vivo* large-scale cortical mapping using channelrhodopsin-2

stimulation in transgenic mice reveals asymmetric and reciprocal relationships between cortical areas. *Front. Neural Circuits* 6:11. doi: 10.3389/fncir.2012.00011

Lin, J. Y., Lin, M. Z., Steinbach, P., and Tsien, R. Y. (2009). Characterization of engineered channelrhodopsin variants with improved properties and kinetics. *Biophys. J.* 96, 1803–1814. doi: 10.1016/j.bpj.2008.11.034

Maguire, E. A. (2001). The retrosplenial contribution to human navigation: a review of lesion and neuroimaging findings. *Scand. J. Psychol.* 42, 225–238. doi: 10.1111/1467-9450.00233

Manita, S., Suzuki, T., Homma, C., Matsumoto, T., Odagawa, M., Yamada, K., et al. (2015). A top-down cortical circuit for accurate sensory perception. *Neuron* 86, 1304–1316. doi: 10.1016/j.neuron.2015.05.006

Mao, T., Kusefoglu, D., Hooks, B. M., Huber, D., Petreanu, L., and Svoboda, K. (2011). Long-range neuronal circuits underlying the interaction between sensory and motor cortex. *Neuron* 72, 111–123. doi: 10.1016/j.neuron.2011.07.029

Miesenböck, G. (2009). The optogenetic catechism. *Science* 326, 395–399. doi: 10.1126/science.1174520

Miller, K. D. (2016). Canonical computations of cerebral cortex. *Curr. Opin. Neurobiol.* 37, 75–84. doi: 10.1016/j.conb.2016.01.008

Minoshima, S., Giordani, B., Berent, S., Frey, K. A., Foster, N. L., and Kuhl, D. E. (1997). Metabolic reduction in the posterior cingulate cortex in very early Alzheimer's disease. *Ann. Neurol.* 42, 85–94. doi: 10.1002/ana.410420114

Mišić, B., and Sporns, O. (2016). From regions to connections and networks: new bridges between brain and behavior. *Curr. Opin. Neurobiol.* 40, 1–7. doi: 10.1016/j.conb.2016.05.003

Nagel, G., Brauner, M., Liewald, J. F., Adeishvili, N., Bamberg, E., and Gottschalk, A. (2005). Light activation of channelrhodopsin-2 in excitable cells of *Caenorhabditis elegans* triggers rapid behavioral responses. *Curr. Biol.* 15, 2279–2284. doi: 10.1016/j.cub.2005.11.032

Nagel, G., Szellas, T., Huhn, W., Kateriya, S., Adeishvili, N., Berthold, P., et al. (2003). Channelrhodopsin-2, a directly light-gated cation-selective membrane channel. *Proc. Natl. Acad. Sci. U.S.A.* 100, 13940–13945. doi: 10.1073/pnas.1936192100

Nowak, L. G., and Bullier, J. (1998). Axons, but not cell bodies, are activated by electrical stimulation in cortical gray matter. II. Evidence from selective inactivation of cell bodies and axon initial segments. *Exp. Brain Res.* 118, 489–500. doi: 10.1007/s002210050305

Oh, S. W., Harris, J. A., Ng, L., Winslow, B., Cain, N., Mihalas, S., et al. (2014). A mesoscale connectome of the mouse brain. *Nature* 508, 207–214. doi: 10.1038/nature13186

Park, H. J., and Friston, K. (2013). Structural and functional brain networks: from connections to cognition. *Science* 342:1238411. doi: 10.1126/science.1238411

Petreanu, L., Huber, D., Sobczyk, A., and Svoboda, K. (2007). Channelrhodopsin-2-assisted circuit mapping of long-range callosal projections. *Nat. Neurosci.* 10, 663–668. doi: 10.1038/nn1891

Petreanu, L., Mao, T., Sternson, S. M., and Svoboda, K. (2009). The subcellular organization of neocortical excitatory connections. *Nature* 457, 1142–1145. doi: 10.1038/nature07709

Petrof, I., Viaene, A. N., and Sherman, S. M. (2015). Properties of the primary somatosensory cortex projection to the primary motor cortex in the mouse. *J. Neurophysiol.* 113, 2400–2407. doi: 10.1152/jn.00949.2014

Raastad, M., and Shepherd, G. M. G. (2003). Single-axon action potentials in the rat hippocampal cortex. *J. Physiol. (Lond).* 548, 745–752. doi: 10.1113/jphysiol.2002.032706

Reinhold, K., Lien, A. D., and Scanziani, M. (2015). Distinct recurrent versus afferent dynamics in cortical visual processing. *Nat. Neurosci.* 18, 1789–1797. doi: 10.1038/nn.4153

Rolls, E. T. (2016). *Cerebral Cortex: Principles of Operation.* Oxford: Oxford University Press.

Sabatini, B. L., and Regehr, W. G. (1999). Timing of synaptic transmission. *Annu. Rev. Physiol.* 61, 521–542. doi: 10.1146/annurev.physiol.61.1.521

Sato, T. K., Häusser, M., and Carandini, M. (2014). Distal connectivity causes summation and division across mouse visual cortex. *Nat. Neurosci.* 17, 30–32. doi: 10.1038/nn.3585

Sleigh, J., Harvey, M., Voss, L., and Denny, B. (2014). Ketamine - more mechanisms of action than just NMDA blockade. *Trends Anaesth. Critic. Care* 4, 76–81. doi: 10.1016/j.tacc.2014.03.002

Sreenivasan, V., Esmaeili, V., Kiritani, T., Galan, K., Crochet, S., and Petersen, C. C. (2016). Movement initiation signals in mouse whisker motor cortex. *Neuron* 92, 1368–1382. doi: 10.1016/j.neuron.2016.12.001

Sugar, J., Witter, M. P., van Strien, N. M., and Cappaert, N. L. (2011). The retrosplenial cortex: intrinsic connectivity and connections with the (para)hippocampal region in the rat. An interactive connectome. *Front Neuroinform* 5:7. doi: 10.3389/fninf.2011.00007

Suter, B. A., Migliore, M., and Shepherd, G. M. G. (2013). Intrinsic electrophysiology of mouse corticospinal neurons: a class-specific triad of spike-related properties. *Cereb. Cortex* 23, 1965–1977. doi: 10.1093/cercor/bhs184

Suter, B. A., and Shepherd, G. M. G. (2015). Reciprocal interareal connections to corticospinal neurons in mouse m1 and s2. *J. Neurosci.* 35, 2959–2974. doi: 10.1523/JNEUROSCI.4287-14.2015

Vann, S. D., Aggleton, J. P., and Maguire, E. A. (2009). What does the retrosplenial cortex do? *Nat. Rev. Neurosci.* 10, 792–802. doi: 10.1038/nrn2733

Wark, B., Lundstrom, B. N., and Fairhall, A. (2007). Sensory adaptation. *Curr. Opin. Neurobiol.* 17, 423–429. doi: 10.1016/j.conb.2007.07.001

Wu, M. C., David, S. V., and Gallant, J. L. (2006). Complete functional characterization of sensory neurons by system identification. *Annu. Rev. Neurosci.* 29, 477–505. doi: 10.1146/annurev.neuro.29.051605.113024

Yamawaki, N., Radulovic, J., and Shepherd, G. M. G. (2016). A corticocortical circuit directly links retrosplenial cortex to M2 in the mouse. *J. Neurosci.* 36, 9365–9374. doi: 10.1523/JNEUROSCI.1099-16.2016

Yamawaki, N., and Shepherd, G. M. G. (2015). Synaptic circuit organization of motor corticothalamic neurons. *J. Neurosci.* 35, 2293–2307. doi: 10.1523/JNEUROSCI.4023-14.2015

Yang, W., Carrasquillo, Y., Hooks, B. M., Nerbonne, J. M., and Burkhalter, A. (2013). Distinct balance of excitation and inhibition in an interareal feedforward and feedback circuit of mouse visual cortex. *J. Neurosci.* 33, 17373–17384. doi: 10.1523/JNEUROSCI.2515-13.2013

Zingg, B., Hintiryan, H., Gou, L., Song, M. Y., Bay, M., Bienkowski, M. S., et al. (2014). Neural networks of the mouse neocortex. *Cell* 156, 1096–1111. doi: 10.1016/j.cell.2014.02.023